Journal of Ocean Engineering and Marine Energy (2020) 6:157–169
https://doi.org/10.1007/s40722-020-00165-9

RESEARCH ARTICLE

Statistical linearization of the Morison's equation applied to wave energy converters

Leandro S. P. da Silva[1] · Benjamin S. Cazzolato[1] · Nataliia Y. Sergiienko[1] · Boyin Ding[1] · Helio M. Morishita[2] · Celso P. Pesce[3]

Received: 19 February 2020 / Accepted: 13 May 2020 / Published online: 10 June 2020

Abstract
The viscous drag acting on wave energy converters may have a significant effect on the dynamics during high-energetic sea states and large motions experienced due to resonance. The viscous drag is a nonlinear phenomenon of floating systems usually modelled based on the Morison's equation using the relative velocity between the structure and the wave particle. To include such a nonlinearity into the system dynamics, nonlinear time domain simulations are generally employed, which are computationally expensive compared to frequency domain simulations. To overcome this problem, this work presents the derivation of the viscous drag force/torque under the statistical linearization technique using the frequency domain model. The technique offers a reliable tool for the estimation of the system dynamics while maintaining a low computational cost when compared to time domain simulations. For the proposed nonlinearity, the resulting equivalent linear term can be decomposed into two components: an excitation term and a damping term. To illustrate the applicability of the derivation, two conceptually different wave energy converters are investigated: a heaving point absorber, and an oscillating wave surge converter. The results obtained using statistical linearization are compared to their respective nonlinear time domain simulations to verify the reliability of the technique. Also, a comparison between the statistical linearization results using the relative motion and using only the structure motion is presented to illustrate the importance of including the relative velocity for wave energy applications. Excellent agreements have been obtained between statistical linearization model using the relative motion and its respective nonlinear time domain model for both devices in terms of spectral content, probability density of the velocity components, and energy absorbed by the device.

Keywords Morison's equation · Statistical linearization · Relative motion · Frequency domain

1 Introduction

Some concepts of wave energy converters (WECs) are often designed to operate in resonance with the incoming wave field to improve the energy conversion efficiency, leading to large displacements. As a result, some nonlinearities play a significant contribution to the system response and must be accounted for in the numerical models. The viscous drag can have a significant impact depending on the type of device (Giorgi and Ringwood 2018; Giorgi et al. 2016; Todalshaug et al. 2011). The representation of the viscous drag is usually formulated based on Morison's equation (Morison et al. 1950), which is a quadratic function of the relative velocity between the structure and the wave particle. The magnitude of the viscous drag depends on the shape and size of the device, operating condition, and characteristics of the incident wave (spectral formulation, significant wave height, wave peak period).

Generally, time domain (TD) models are built to analyze the dynamics of WECs subjected to nonlinear loads, such as the viscous drag (Babarit et al. 2012). However, these analyses are computationally expensive compared to traditional frequency domain (FD) models, which may be unfeasible to analyze the dynamics across different sea states or for

✉ Leandro S. P. da Silva
leandro.dasilva@adelaide.edu.au

[1] School of Mechanical Engineering, The University of Adelaide, Adelaide, SA, Australia

[2] Escola Politécnica, Department of Naval Architecture and Ocean Engineering, University of São Paulo, São Paulo, SP, Brazil

[3] Escola Politécnica, Offshore Mechanics Laboratory, University of São Paulo, São Paulo, SP, Brazil

optimization routines using several variables. Especially at preliminary design stages, numerical models of WECs must be suitable for automatic optimization. Such models must produce reliable results, have flexible applications, and have a low computational cost (Davidson and Costello 2020). Based on those requirements, an appropriated approach to estimate the response of the nonlinear system is to apply statistical linearization (SL). The SL offers a fast and reliable estimation of the system stationary response under stochastic loads (wave, earthquake and wind forces) (Roberts and Spanos 2003), and has been successfully applied to various WECs (Silva et al. 2020a), and for several optimization routines of a multi-mode WEC under various sea states and parameters (Sergiienko et al. 2020). Built upon the FD model, the technique consists in replacing the nonlinear equation by its equivalent linear one, where the difference is usually minimized in a mean square sense.

The linearization of Morison's equation has been applied to offshore structures (Naess and Pisano 1997; Wolfram 1999). Some of the analyses simplify the nonlinear drag based on the assumption of small velocity of the structure compared to the fluid flow, which is assumed valid for such an application. Regarding WECs, previous works using SL have also simplified viscous drag force, in this case, using only the velocity of the structure measured with respect to Earth (Silva et al. 2020a; Silva 2019; Folley 2016; Folley and Whittaker 2010). However, the velocity of the structure with respect to the fluid flow is important in wave energy applications, because the wave velocity and structure velocity may have the same order of magnitude. As a result, the main contributions of this paper are as follows: (1) to demonstrate the formalization of the Morison's equation using the SL technique by introducing the relative motion between the structure and the wave field; and (2) to demonstrate the importance of including the wave velocity into the calculation of the viscous drag force for different types of WECs.

The paper is structured as follows. First, a brief description of ocean waves based on the linear wave theory is given in Sect. 2. Subsequently, Sect. 3 presents the FD modelling, the nonlinear viscous drag force/torque, and its linearization. Then the technique is applied to two conceptually different wave energy devices, (a) a heaving point absorber (PA) (in Sect. 4), and (b) an oscillating wave surge converter (OWSC) (in Sect. 5), both illustrated in Fig. 1. The SL technique is compared with its respective nonlinear TD simulation to verify the reliability of the technique for these applications. Also, a comparison with the SL results using only the body motion for the viscous drag is investigated to demonstrate the importance of including the relative motion. Finally, a discussion about the applicability of the technique and main results are summarized.

2 Ocean waves

This section describes relevant wave properties to calculate the viscous drag component. The ocean waves are here described based on the well-known linear wave theory. This allows the superposition of elementary results, such as wave elevations

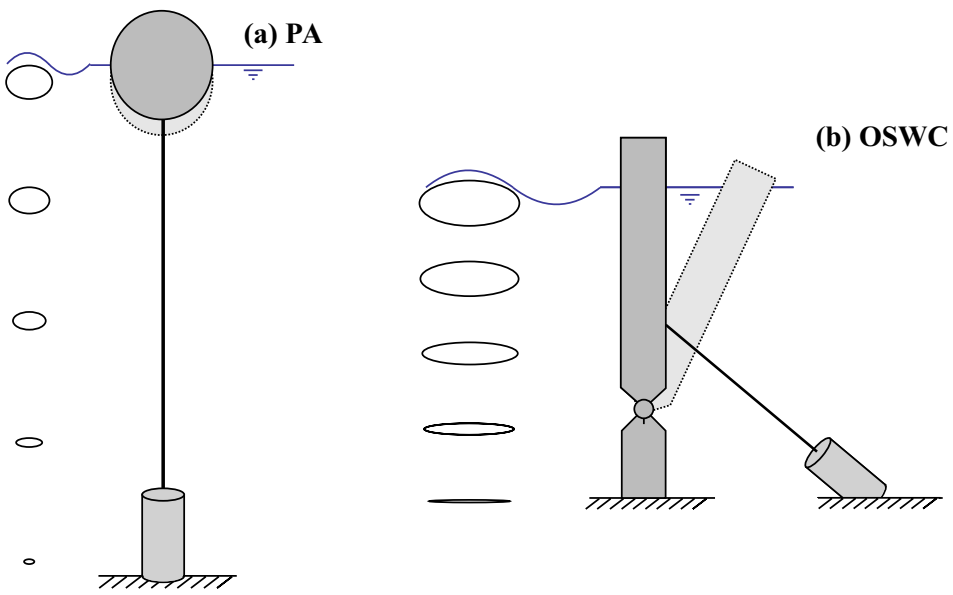

Fig. 1 Trajectory of wave particles at different water depths and two conceptually different WECs (point absorber and oscillating wave surge converter) under viscous drag loads

and velocities, which is essential for the characterization of real sea states. The wave velocity is presented using a single frequency component. However, further analysis is based on the spectral representation of the sea state. For a fixed position of the horizontal sea plane, the wave surface elevation can be described as:

$$\zeta(t) = \mathfrak{Re}\{\zeta_a\, e^{i\omega t}\}, \tag{1}$$

where ζ_a denotes the magnitude of the wave complex amplitude, and ω is the wave frequency. The wave-particle velocities ($\dot{q}_\zeta$) located at the submerged depth z_{sub} in the horizontal (u) and vertical (w) directions are given, respectively, by Journée and Massie (2000):

$$\begin{aligned}\dot{q}_{\zeta,u}(z_{\text{sub}},t) &= \mathfrak{Re}\left\{\omega\zeta_a \frac{\cosh(k(h+z_{\text{sub}}))}{\sinh(kh)}\, e^{i\omega t}\right\} \\ &= \mathfrak{Re}\left\{\hat{C}_{\zeta,u}(\omega)\zeta_a e^{i\omega t}\right\},\end{aligned} \tag{2}$$

$$\begin{aligned}\dot{q}_{\zeta,w}(z_{\text{sub}},t) &= \mathfrak{Re}\left\{i\omega\zeta_a \frac{\sinh(k(h+z_{\text{sub}}))}{\sinh(kh)}\, e^{i\omega t}\right\} \\ &= \mathfrak{Re}\left\{\hat{C}_{\zeta,w}(\omega)\zeta_a e^{i\omega t}\right\},\end{aligned} \tag{3}$$

where h is the water depth, $\hat{C}_\zeta$ is a transfer function that relates the wave velocity at a specified location and the wave surface elevation, and k is the wavenumber. The wavenumber is obtained based on the linear dispersion relation as Newman (2018):

$$\omega^2 = gk\tanh(kh). \tag{4}$$

3 Frequency domain analysis

In the conventional hydrodynamic approach, the frequency domain analysis is carried out in terms of response amplitude operators (RAO). In such models, the dynamics are given by a set of linearized equations, in which the RAO is a transfer function that relates the body response and the wave surface elevation. For simplicity, the following analysis is applied to a single DOF system; however, it can be extended to systems with multiple DOFs. Assuming a harmonic response of the system due to the characteristics of the excitation, the response can be described by:

$$q(t) = \mathfrak{Re}\{\hat{q}_a\, e^{i\omega t}\}, \tag{5}$$

where $\hat{q}_a$ is the complex amplitude of the generalized coordinate q. Based on the generalized coordinate and its time derivatives, the RAO may be written in FD as:

$$\begin{aligned}\text{RAO}_\text{q} &= \frac{\hat{q}_\text{a}}{\zeta_\text{a}} \\ &= \frac{\hat{F}_w(\omega)}{-\omega^2[M + A(\omega)] + i\omega\left[B(\omega) + B_{\text{pto}}\right] + K},\end{aligned} \tag{6}$$

where M is the mass (or moment of inertia), B_{pto} is the power-take-off (PTO) damping, and K denotes all stiffness components (mechanical and hydrostatic); $\hat{F}_w(\omega)$ represents the complex wave excitation force per unit of wave amplitude; $A(\omega)$ and $B(\omega)$ are the well-known quantities of hydrodynamic added mass (or moment of inertia) and radiation damping, respectively. For a single DOF system, the spectral response of the body displacement as a function of the RAO and spectrum of wave elevation, $S_{\zeta_a}(\omega)$, can be calculated as:

$$S_\text{q}(\omega) = |\text{RAO}_q|^2 S_{\zeta_a}(\omega), \tag{7}$$

and the average power absorbed by the linear PTO system as Silva et al. (2020a):

$$P_{\text{pto}} = B_{\text{pto}}\sigma_{\dot{q}}^2, \tag{8}$$

where $\sigma_{\dot{q}}$ denotes the standard deviation of the WEC velocity $\dot{q}$.

3.1 Drag force-Morison's equation

Linear potential wave theory assumes inviscid fluid and thus neglects the effects of viscous forces/torque acting on the WEC. Therefore, the inclusion of a drag force is required to improve the estimation of the body response. In this regard, this work represents the viscous drag component in the TD based on the Morison's equation (Morison et al. 1950), in which the force is proportional to the relative velocity squared, and the absolute sign preserves the force direction:

$$F_\text{d} = -\frac{1}{2}C_\text{D}\rho S_\text{A}|\dot{q}_\text{rel}|\dot{q}_\text{rel}, \tag{9}$$

with:

$$\dot{q}_\text{rel} = \dot{q} - \dot{q}_\zeta, \tag{10}$$

where C_D and S_A denote the drag coefficient and the cross-sectional area of the structure perpendicular to the relative motion respectively; $\dot{\hat{q}}_\text{rel}$ is the relative velocity between the structure and the undisturbed wave-particle velocity, where Eq. (2) describes the wave velocity for the vertical direction (u) and Eq. (3) for the horizontal direction (w). Based on the nonlinear viscous drag force, an equivalent linear force can be represented using SL as:

$$F_\text{d} = -D_\text{m}\dot{\hat{q}}_\text{rel}, \tag{11}$$

where D_m is the linearized drag coefficient.

The difference between the nonlinear drag term and its equivalent linear one is minimized based on the SL procedure Berge and Penzien (1974):

$$D_{\mathrm{m}} = \frac{\left\langle \frac{1}{2} C_{\mathrm{D}} \rho S_{\mathrm{A}} |\dot{q}_{\mathrm{rel}}| \dot{q}_{\mathrm{rel}}^2 \right\rangle}{\left\langle \dot{q}_{\mathrm{rel}}^2 \right\rangle}, \tag{12}$$

where $\langle\ \rangle$ denotes the mathematical expectation.

Assuming a random process described by a Gaussian distribution, the probability density function (PDF) for the relative velocity can be written as:

$$f(\dot{q}_{\mathrm{rel}}) = \frac{1}{\sigma_{\dot{q}_{\mathrm{rel}}}\sqrt{2\pi}} \exp\left(-\frac{\dot{q}_{\mathrm{rel}}^2}{2\sigma_{\dot{q}_{\mathrm{rel}}}^2} \right), \tag{13}$$

where $\sigma_{\dot{q}_{\mathrm{rel}}}$ denotes the standard deviation of the relative velocity $\dot{q}_{\mathrm{rel}}$. Based on the Gaussian distribution, the solution of Eq. (12) is given by Berge and Penzien (1974):

$$D_{\mathrm{m}} = \frac{1}{2} C_{\mathrm{D}} \rho S_{\mathrm{A}} \sqrt{\frac{8}{\pi}} \sigma_{\dot{q}_{\mathrm{rel}}}. \tag{14}$$

Thus, the equivalent linear term requires only the standard deviation of the relative velocity. Substituting Eqs. (10) into (11), the linearized form of Eq. (9) can be rewritten into two terms, one corresponding to the body drag force that depends on the body velocity (damping) and the second corresponding to the wave drag force that depends on the wave field velocity (excitation):

$$F_{\mathrm{d,b}} + F_{\mathrm{d,w}} = -D_{\mathrm{m}} \dot{\hat{q}}_a + D_{\mathrm{m}} \dot{\hat{q}}_\zeta. \tag{15}$$

Equation (15) can be modified and included into the equivalent RAO as:

$$\mathrm{RAO}_{\mathrm{q,eq}} = \frac{\hat{q}_{\mathrm{a}}}{\zeta_{\mathrm{a}}} = \frac{\hat{F}_w(\omega) + D_m \hat{C}_{\zeta,\dot{q}}}{-\omega^2[M + A(\omega)] + i\omega\left[B(\omega) + B_{\mathrm{pto}} + D_{\mathrm{m}}\right] + K}, \tag{16}$$

where $\hat{C}_{\zeta,\dot{q}}$ relates the wave surface elevation and wave-particle velocity, as shown in Equations (2) and (3), which is multiplied by the linear drag coefficient D_m to represent the wave drag contribution. The equivalent spectral response of the body displacement is obtained from Eq. (7).

In the equivalent RAO, the spectrum of relative velocity is required to calculate the standard deviation, as shown in Eq. (14), which is used in the equivalent drag damping and drag excitation force. In this regard, the complex amplitude of the equivalent relative velocity between the body velocity and wave particle, in Eq. (10), can be formulated as:

$$\dot{\hat{q}}_{\mathrm{rel}} = i\omega \mathrm{RAO}_{\mathrm{q,eq}} \zeta_{\mathrm{a}} - \hat{C}_{\zeta,\dot{q}} \zeta_{\mathrm{a}}. \tag{17}$$

Therefore, a transfer function can be established to relate the equivalent relative velocity to the wave amplitude:

$$\mathrm{RAO}_{\dot{q}_{\mathrm{rel}},\mathrm{eq}} = \frac{\dot{\hat{q}}_{\mathrm{rel}}}{\zeta_{\mathrm{a}}} = i\omega \mathrm{RAO}_{\mathrm{q,eq}} - \hat{C}_{\zeta,\dot{q}}, \tag{18}$$

where the spectral response of the relative velocity is obtained as:

$$S_{\dot{q}_{\mathrm{rel}}}(\omega) = |\mathrm{RAO}_{\dot{q}_{\mathrm{rel}},\mathrm{eq}}|^2 S_{\zeta_{\mathrm{a}}}(\omega), \tag{19}$$

and the standard deviation of the relative velocity is obtained as:

$$\sigma_{\dot{q}_{\mathrm{rel}}}^2 = \int_0^\infty S_{\dot{q}_{\mathrm{rel}}}(\omega) d\omega. \tag{20}$$

The equivalent linear terms require the knowledge of the body response, as shown in Eq. (12). However, the response distribution is not initially known. Based on that, an iterative procedure is generally applied, in which the linear system is used as an initial guess. This iterative procedure runs using the response of the previous iteration until the solution achieves a predetermined convergence criterion. For some examples of iterative procedure applied for WECs, see Silva et al. (2020a) and Silva (2019). To demonstrate the technique, the linearization of the Morison's equation is applied to two conceptually different WECs: a floating PA constrained to move in heave only, and an OWSC that pitches around a hinged connection, as shown Fig. 1.

4 Point absorber

The first device investigated is a floating spherical PA with a radius, R, which is assumed to move only in the heave direction, $q(t) = z(t)$. The structure is connected to a linear PTO, and the only source of nonlinearity considered comes from the drag force, where the vertical wave velocity is calculated using Eq. (3). However, other nonlinear effects can be included into the system dynamics using the SL technique, as shown in Silva et al. (2019, 2020a), Spanos et al. (2016). For the system described, the equivalent transfer function between the body displacement and wave elevation, $RAO_{z,eq}$, can be calculated based on Eq. (16) as:

$$\mathrm{RAO}_{\mathrm{z,eq}} = \frac{\hat{\hat{z}}}{\zeta_{\mathrm{a}}} = \frac{\hat{F}_w(\omega) + D_{\mathrm{m}} \hat{C}_{\zeta,\mathrm{w}}}{-\omega^2[M + A(\omega)] + i\omega[B(\omega) + B_{\mathrm{pto}} + D_{\mathrm{m}}] + K}. \tag{21}$$

Similarly, the equivalent transfer function between the relative velocity and the wave elevation can be estimated using Eq. (21) as:

$$\mathrm{RAO}_{\dot{q}_{\mathrm{rel}},\mathrm{eq}} = \frac{\dot{\hat{q}}_{\mathrm{rel}}}{\zeta_{\mathrm{a}}} = i\omega \mathrm{RAO}_{\mathrm{z,eq}} - \hat{C}_{\zeta,\mathrm{w}}, \tag{22}$$

and the power absorbed calculated as:

$$P_{\mathrm{pto}} = B_{\mathrm{pto}}\sigma_{\dot{z}}^2. \tag{23}$$

The drag coefficient of the floating PA can be estimated based on the Keulegan–Carpenter number *KC*, which is a dimensionless quantity for oscillatory flow that describes the importance of the ratio between the drag and inertia loads (Keulegan and Carpenter 1956). For a single frequency motion, the *KC* number is defined as:

$$KC = 2\pi\frac{q_a}{L_c}, \tag{24}$$

where q_{a} denotes the amplitude of the body motion, and L_{c} is the characteristic length of the object, which for the sphere is equal to the diameter. For the floating PA, the *KC* is expected to be within the range of 0–6. According to Molin (2002), the drag coefficient is around 0.5 to 1 for this range. For the following analysis, the C_{D} is assumed to be equal to 1. However, this estimation of drag coefficient is subjected to uncertainties, in which the effects on the system dynamics can be estimated using sensitive analysis as in Todalshaug et al. (2011). Note that the mentioned source of uncertainty is associated with the value of the drag coefficient used in the analysis, and not with the SL method itself.

The main parameters used during the simulations are described in Table 1. The natural period, T_{n}, of the PA is set to 7.5 s by tuning the total stiffness of the system. The hydrodynamic coefficients of added mass and radiation damping are obtained using the open-source code NEMOH (Babarit and Delhommeau 2015). Nonlinear TD simulations were performed to verify the reliability of the technique. For TD simulations, the radiation force is replaced by an equivalent transfer function, as described in Perez and Fossen (2009). The PTO damping is set to operate in an optimal condition for the specified stiffness and device specifications, as shown in Fig. 11 in Appendix.

Table 1 Simulation parameters (PA)

Property	Value	Units
K	1000	[kN/m]
B_{pto}	250	[kN s/m]
M	1828	[kg]
h	50	[m]
R	5	[m]
C_{D}	1	[−]

The incident wave field is assumed to be described by a JONSWAP spectrum with peak enhancement factor, γ, equal to 3.3; and the peak period, T_p, varies from 5 to 15 s to be within the range of the natural period of the PA, while the significant wave height, H_s, is 3 m. The wave spectrum is constructed from 300 frequency components from 0.25 to 2.5 rad/s. For each sea state, 10 sets of phase angles are used to generate the wave components in TD simulations; each of them contained approximately 300 cycles. Note that the results of the following analysis are sensitive to the operating condition (PTO coefficients) and sea state, such as spectral formulation, significant wave height and peak wave period.

Figure 2 shows the time series of the wave velocity ($\dot{q}_{\zeta,\mathrm{w}}$), body velocity ($\dot{z}$), and their relative velocity ($\dot{z} - \dot{q}_{\zeta,\mathrm{w}}$) for the first 200 s ($T_p = 7.5$ s and $H_s = 3$ m), where the undisturbed wave velocity is calculated at the center of the sphere. At this condition, the body is resonating with the incoming wave field, and the magnitude of the body and wave velocities are comparable, which makes the relative velocity important. Figure 3 shows the probability distribution of the velocities obtained from the TD data, such as in Fig. 2, considering the entire time series and different sets of phase angles of each sea state. The TD results (asterisk) are compared with the PDF estimations using SL (solid line) based on a Gaussian distribution.

As it can be observed in Fig. 3, the Gaussian assumption can be used to describe the probability of velocity distribution, given in Eq. (13). The estimations using SL are comparable to the nonlinear TD simulations. Note that an accurate representation of the probability distribution of the relative velocity is required for a reliable estimation of the response and drag contribution coefficient, D_m, which assumes a Gaussian distribution, see Eq. (14).

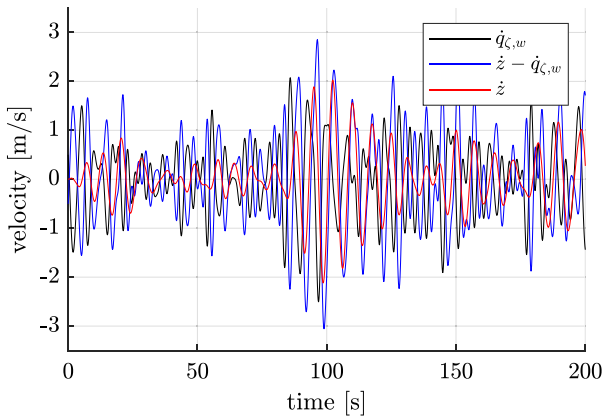

Fig. 2 Time series of the velocities at resonance ($T_{\mathrm{p}} = 7.5$ s and $H_{\mathrm{s}} = 3$ m)

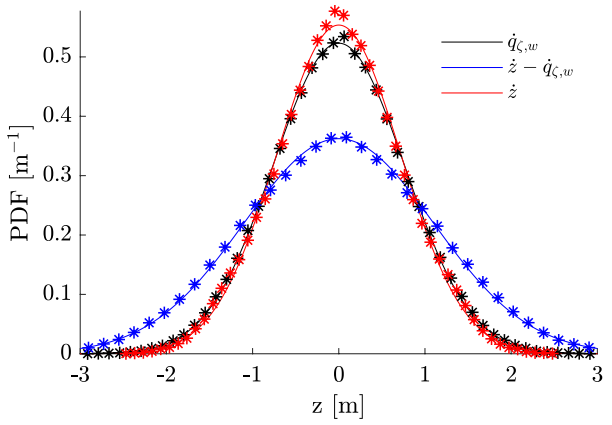

Fig. 3 Time series data and PDF of the velocities at resonance (T_p = 7.5 s and H_s = 3 m). The asterisk denotes the probability density obtained from TD data, while the solid line denotes the SL results

To demonstrate the relevance of each velocity component, namely the wave velocity ($\dot{q}_{\zeta,w}$), body velocity ($\dot{z}$), and relative velocity ($\dot{z} - \dot{q}_{\zeta,w}$), Fig. 4 illustrates the power spectral density (PSD) of the velocities across three sea states close to resonance, T_p = 6, 7.5, 9 s and H_s = 3 m. The solid line refers to SL results, while the shaded area contains the mean and standard deviations from TD simulations. For the three sea states simulated, the velocities using SL and TD follow a good agreement and the relative wave velocity shows to be important for the conditions simulated, Fig. 4a–c. The phase between the body and wave velocities affects the magnitude of the complex relative velocity, this effect can be noticed by observing the spectral magnitude over the frequency components. For the sea state with period lower than the resonance, Fig. 4a, the body and wave velocities are almost out-of-phase and the magnitude of the relative velocity increases; while for the sea state, with period higher than the resonance, Fig. 4c, the components are in-phase and the magnitude is reduced at some frequencies.

To investigate the importance of the vertical wave velocity in the formulation, four different approaches are considered: nonlinear TD with relative velocity, SL with relative velocity ($\dot{z} - \dot{q}_{\zeta,w}$), SL where the wave velocity is neglected ($\dot{z}$), and the linear FD model (no viscous drag included), which is illustrated in Fig. 5. This comparison is important in order to validate the results obtained using SL, while investigates the contribution of the relative velocity against its simplified SL model using only the body motion. Note that for the SL results using only the body motion, no excitation drag term exists, and a different converged solution is achieved.

In general, the SL with relative velocity and TD results revealed good agreement for all sea states investigated, having the same spectral response over all frequency

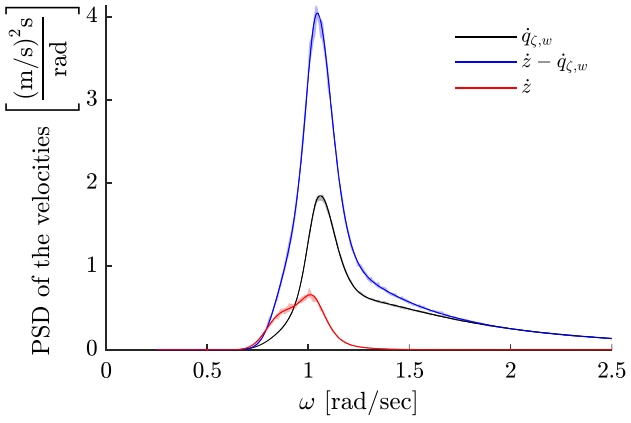

(a) PSD of the vertical velocities (T_p = 6 s).

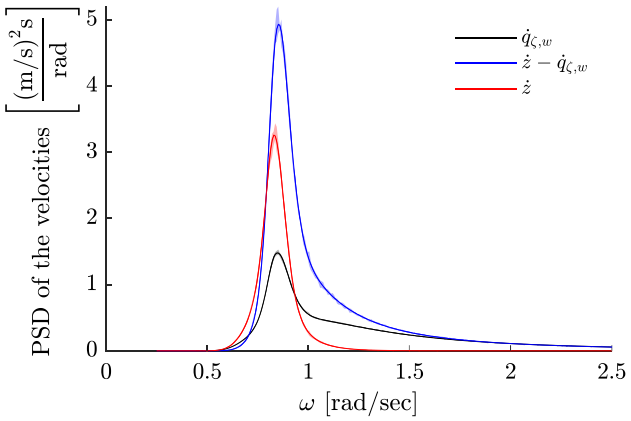

(b) PSD of the vertical velocities (T_p = 7.5 s).

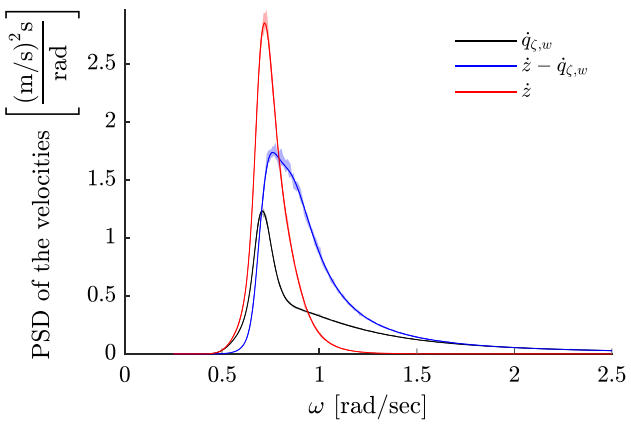

(c) PSD of the vertical velocities (T_p = 9 s).

Fig. 4 PSD of the velocities for three T_p (6, 7.5, 9 s) and a H_s = 3 m. The solid line refers to the SL results, and the shaded area contains the mean and standard deviation of the TD simulations

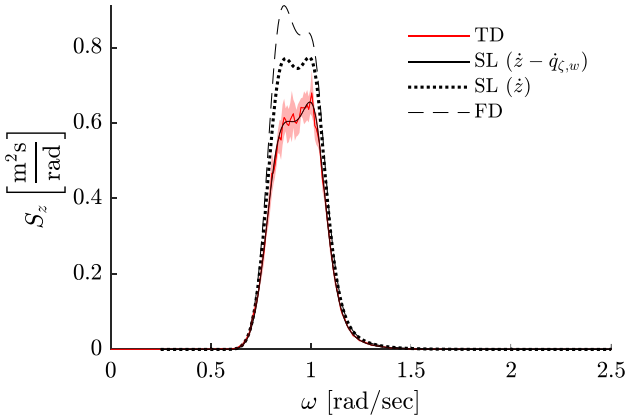

(a) PSD of vertical displacement ($T_p = 6\,\text{s}$).

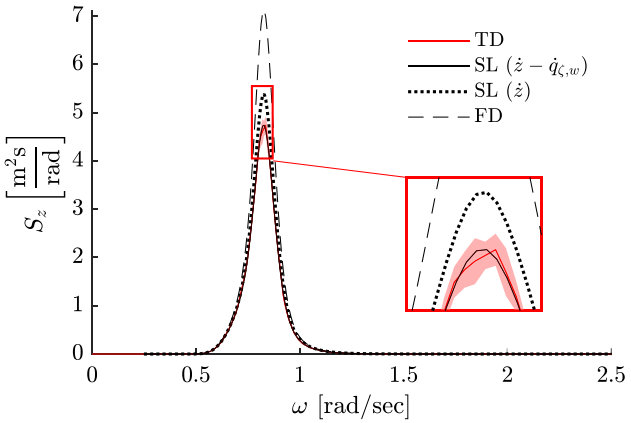

(b) PSD of the vertical displacement ($T_p = 7.5\,\text{s}$).

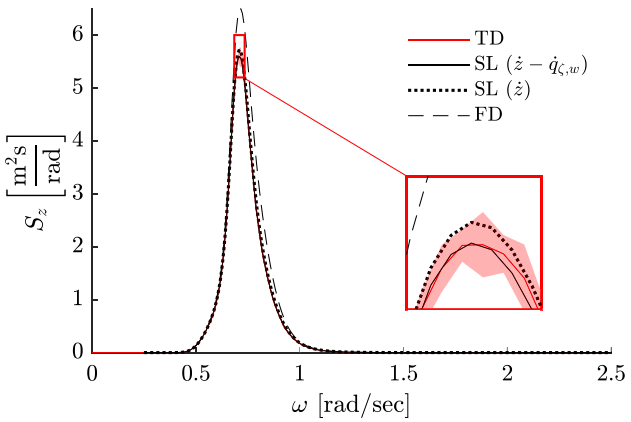

(c) PSD of the vertical displacement ($T_p = 9\,\text{s}$).

Fig. 5 PSD of the displacement for three T_p (6, 7.5, 9 s) and a $H_\text{s} = 3$ m. The shaded area denotes the standard deviation of the TD simulations

components. As expected, discrepancies with the FD model are higher at the resonance, where the body has higher motions and the drag contribution increases, see Fig. 5b. The differences between the SL ($\dot{z} - \dot{q}_{\zeta,\text{w}}$) model and SL ($\dot{z}$) occurred mostly for lower periods, Fig. 5a, b, because of the higher wave velocity at higher frequencies. At this velocity, the relative error between the SL ($\dot{z} - \dot{q}_{\zeta,\text{w}}$) model and TD model for the standard deviation of the displacement (σ_z) was less than 1%, while for the SL ($\dot{z}$) model was around 10%, as shown in Fig. 6. At $T_\text{p} = 9$ s, the differences between the SL models are less significant because the device is not resonating, and the wave-particle velocity is smaller, see Fig. 4c. At this velocity, the relative error of σ_z was around 0.1% for the SL ($\dot{z} - \dot{q}_{\zeta,\text{w}}$) model, and 1% for the SL ($\dot{z}$) model, as shown in Fig. 6.

Figure 7 shows the power absorbed by the linear PTO system obtained between the four distinct approaches as a function of the wave period. In general, the SL results

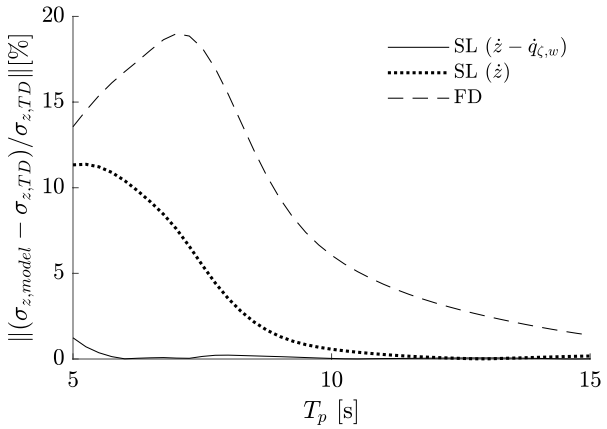

Fig. 6 Relative error between frequency domain-based approaches and the TD simulations for the standard deviation as a function of T_p for a $H_\text{s} = 3$ m

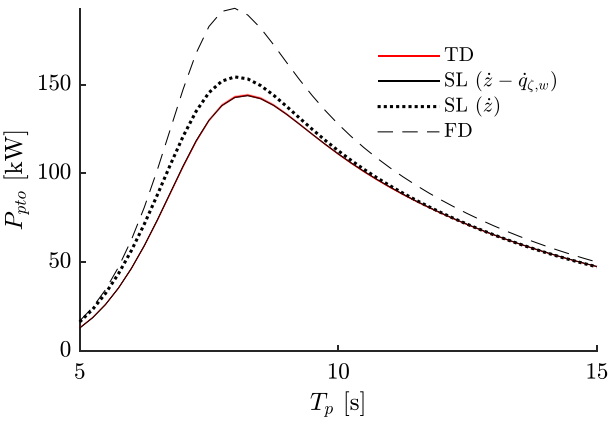

Fig. 7 Power absorbed by the PA as a function of T_p for a $H_\text{s} = 3$ m

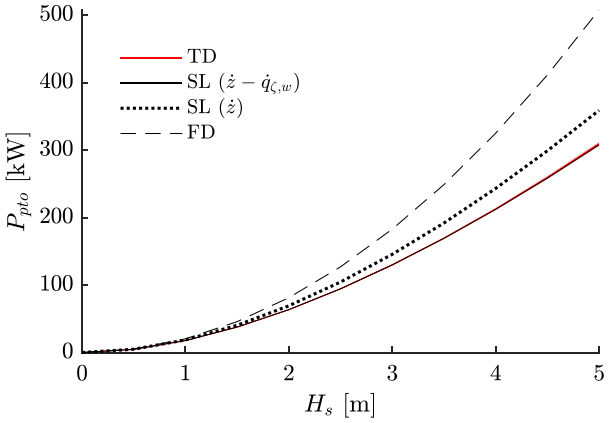

Fig. 8 Power absorbed by the PA as a function of H_s for a $T_p = 7.5$ s

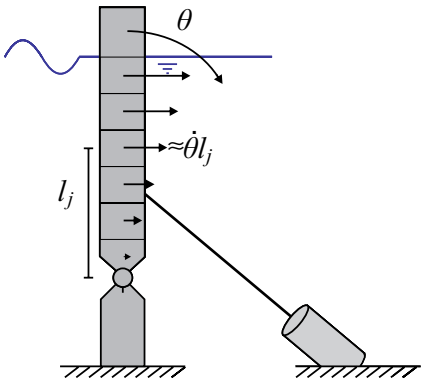

Fig. 9 OWSC, with rotation θ and mean position l_j of the jth section

with relative velocity showed good agreement with the nonlinear TD simulations. The differences between the SL ($\dot{z} - \dot{q}_{\zeta,w}$) and SL ($\dot{z}$) model occurred mostly for T_p lower than 10 s. The power predicted by the SL model using only the body velocity in the drag force formulation is 12.1% ± 6.4% higher than the power calculated using the relative velocity for the range close to resonance ($6\,\text{s} < T_p < 9\,\text{s}$), showing that the damping component of the linear equivalent drag force has more impact on the PA than its excitation component.

A similar trend also occurs over different significant wave heights. Figure 8 shows the power absorbed by the linear PTO system obtained using the four distinct approaches as a function of the wave height and $T_p = 7.5$ s. The viscous drag is a quadratic function of the relative velocity. Hence, its contribution is expected to be relevant at more energetic sea states. However, the importance of including the relative velocity occurred across most of the significant wave heights simulated. For the conditions simulated, the SL ($\dot{z}$) model overestimated the power absorbed by 10.6% ± 4.7% compared to the SL ($\dot{z} - \dot{q}_{\zeta,w}$) model, as shown in Fig. 8. This reinforces the importance of including the relative velocity in the SL model. The results using SL and FD are calculated using the standard deviation, which is obtained by integrating the PSD density of the velocity. Hence, as the spectral distribution of the velocities is small between the two SL models for periods longer than the resonance, the difference in power absorbed is smaller for this range, which occurred at $T_p \geq 9$ s.

5 Oscillating wave surge converter

Consider an OWSC subjected to the nonlinear viscous drag torque, as illustrated in Fig. 9. The generalized coordinate q for this case is equal to the flap angle θ. Besides the viscous drag term, all other torques acting on the OWSC are assumed to be linear. However, additional nonlinearities can be included into the governing equation using SL as shown in Silva et al. (2020a, b). The pitch amplitude (flap angle) is supposed to be sufficiently small, rendering the contribution of vertical drag force components as negligible when compared to that coming from horizontal ones. Therefore, only the horizontal components of the wave-particle velocities are considered. The drag contribution is discretized into N sections along the vertical submerged length of the structure as:

$$M_m = -\sum_{j=1}^{N} D_{m,j} \dot{\hat{q}}_{\text{rel},j}\, l_j, \tag{25}$$

in which each section, j, has an equivalent coefficient and relative velocity given by:

$$D_{m,j} = \frac{1}{2} C_D \rho \Delta S_{A,j} \sqrt{\frac{8}{\pi}} \sigma_{\dot{q}_{rel,j}}, \tag{26}$$

$$\dot{\hat{q}}_{\text{rel},j} = \dot{\hat{\theta}} l_j - \dot{\hat{q}}_{\zeta,uj}, \tag{27}$$

where l_j is the distance between the hinged connection and the center of the section, θ is the flap angle defined in Fig. 9, ΔS_A is the cross-sectional area of the discretized structure, and $j = \{1, 2, \ldots, N\}$ denotes the section index. Based on that, the equivalent RAO can be written as:

$$RAO_{\theta,eq} = \frac{\hat{M}_w(\omega) + \sum_{j=1}^{N} D_{m,j} \hat{C}_{\zeta,uj} l_j}{-\omega^2 [J + A(\omega)] + i\omega [B(\omega) + B_{pto} + \sum_{j=1}^{N} D_{m,j} l_j^2] + K}, \tag{28}$$

Table 2 Simulation parameters (OWSC)

Property	Value	Units
K	33.3×10^3	[kN.m/rad]
B_{pto}	50×10^3	[kN.m.s/rad]
I	5.3×10^6	[kg.m^2]
h	13	[m]
ΔS_A	1.5×26	[m^2]
C_D	8	[−]

where $\hat{M}_w(\omega)$ is the wave excitation torque, J denotes the moment of inertia around the hinged connection, and K accounts for all sources of stiffness components (hydrostatic and PTO). The transfer function that relates the relative velocity between the body and wave velocity for the j section is given by:

$$\mathrm{RAO}_{\dot{q}_{\mathrm{rel},j},eq} = \frac{\dot{q}_{\mathrm{rel},j}}{\zeta_a} = i\omega RAO_{\theta,\mathrm{eq}}\, l_j - \hat{C}_{\zeta,uj}, \tag{29}$$

and the power absorbed calculated as:

$$P_{\mathrm{pto}} = B_{\mathrm{pto}}\sigma^2_{\dot{\theta}}. \tag{30}$$

Like the PA case, the reliability of the proposed formulation is verified using nonlinear TD domain simulations. The selected range of peak wave periods, T_p, varies from 5 to 15 s, and the significant wave height, H_s, is 1.5 m. The main flap width is 26 m, and the main parameters of the OWSC are given in Table 2. The frequency-dependent hydrodynamic coefficients were obtained using the open-source code NEMOH (Babarit and Delhommeau 2015). The natural period of the OWSC is set to 12 s by tuning the total stiffness, and the value of the PTO damping is optimized for the given sea states and device specifications, as shown in Fig. 15 in Appendix. In this paper, the height of the OWSC is discretized using six components ($N = 6$) to illustrate the approach. However, a better discretization must be performed to analyze the effect of the relative wave velocity, which can be compared with the analytical solution using the body velocity as described in Silva et al. (2020a) and Bacelli and Ringwood (2014).

The viscous drag coefficient of the OWSC is estimated using the *KC* number. For the OWSC, the velocity of the top of the flap is consider to in be the same order of magnitude of the wave, which can be verified in Fig. 10c. For such a condition, the *KC* number is generally smaller than unity (Todalshaug et al. 2011). According to the results in Bearman et al. (1985), the viscous drag coefficient for a plate in oscillatory flow in this range is 8. Same value of drag coefficient was used in Giorgi and Ringwood (2018), Todalshaug et al. (2011). However, like the PA case, the drag coefficient is a source of uncertainty. Other sections of the discretized flap operates in a similar *KC* number. Therefore, a single value of drag coefficient is used for all sections.

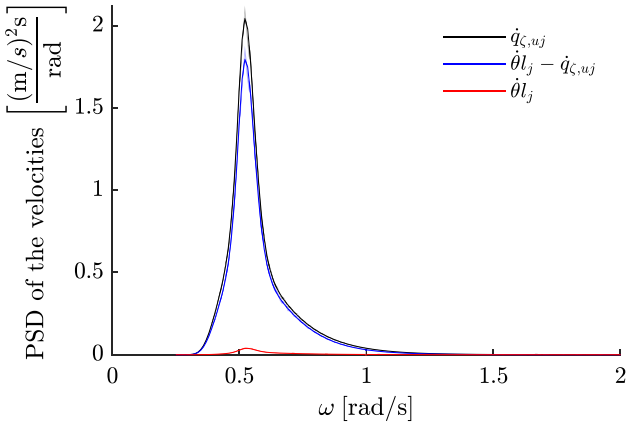

(a) PSD of the horizontal velocities (section $j = 1$).

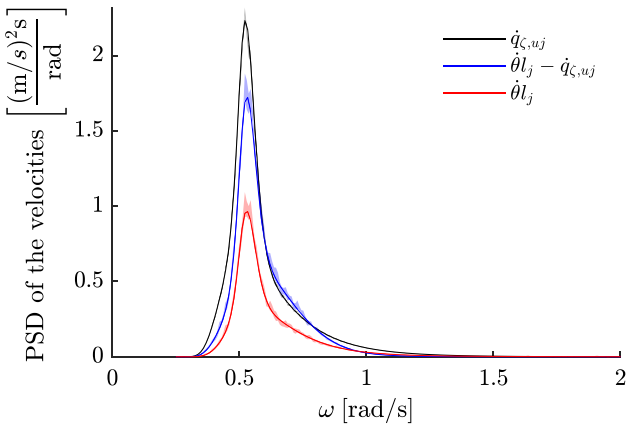

(b) PSD of the horizontal velocities (section $j = 3$).

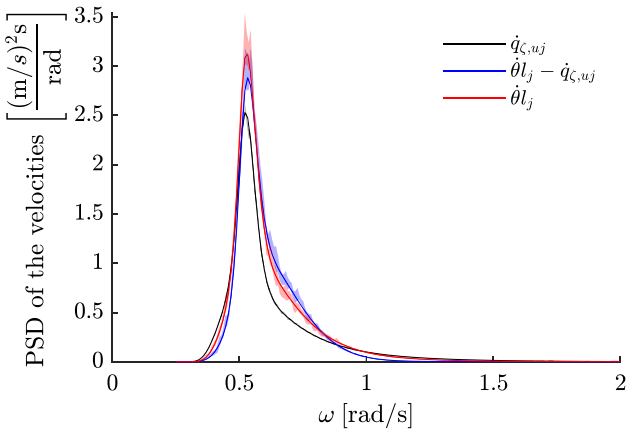

(c) PSD of the horizontal velocities (section $j = 5$).

Fig. 10 PSD of the velocities for sections $j = \{1, 3, 5\}$, $T_\mathrm{p} = 12$ s and $H_s = 1.5$ m. The solid line refers to the SL results, and the shaded area contains the mean and standard deviation of the TD simulations

To demonstrate the contribution of each section in the OWSC, Fig. 10 shows the PSD of the wave velocity ($\dot{q}_{\zeta,uj}$), body velocity ($\dot{\theta} l_j$), and relative velocity ($\dot{\theta} l_j - \dot{q}_{\zeta,uj}$) for three sections ($j = \{1, 3, 5\}$) and assuming the same sea state ($H_s = 1.5$ m and $T_p = 12$ s). The solid line represents the SL results, and the shaded area is the results of TD simulations with standard deviation obtained from 10 runs with different sets of phase angles of the incoming wave. The results obtained using SL and TD are in good agreement for all sections simulated. The wave velocity is calculated around the equilibrium position of each section, whereas the body velocity in the horizontal direction is calculated around the mean position. Therefore, the body velocity in the horizontal direction increases linearly with the position of the section due to the $\dot{\theta} l_j$ relationship, while the magnitude of the wave velocity in the horizontal direction remains almost constant with the depth for the conditions simulated. In general, the wave velocity is more relevant around the hinged connection and exerts an excitation drag term, while at the top, the viscous drag effect is driven by the relative velocity and both damping and excitation terms are of comparable importance.

To investigate the effect of horizontal wave velocity in the formulation, four different approaches are considered: nonlinear TD with relative velocity, SL with relative velocity ($\dot{\theta} l_j - \dot{q}_{\zeta,uj}$), SL with body velocity only ($\dot{\theta} l_j$), and the linear FD model (no viscous drag included). Figure 11 shows the PSD of the angular displacement, θ, using the four different approaches considering the three sea states for $T_p s$ close to resonance. For the nonlinear cases, each section contributes to the total torque. However, the main contribution comes from the viscous drag from the distal end due to its higher magnitude of the force and larger distance from the hinged position. At the distal end, the horizontal velocity of the flap and that of the wave particle are of the same order, see Fig. 10. Therefore, both velocity components must be considered to estimate the drag contribution.

Figure 12 shows the mean power absorbed using the four approaches as a function of the wave period. In general, the results of power absorbed using TD and the SL model with relative velocity are in good agreement, while the SL ($\dot{\theta} l_j$) leads to an underestimate over the entire range of sea states considered. The differences between the SL ($\dot{\theta} l_j - \dot{q}_{\zeta,uj}$) and SL ($\dot{\theta} l_j$) model occurred during the entire range simulated, where the power absorbed predicted by the SL ($\dot{\theta} l_j$) model was $10.3\% \pm 2.0\%$ lower, showing the importance of including the relative velocity over the entire range simulated. As opposed to the PA case, the excitation drag component had a higher impact than the damping drag for the OWSC. This effect of the excitation drag can be associated with the phase between the excitation term, $\hat{M}_w(\omega)$, and the drag term related to the wave action. Also, the wave excitation drag term contribution occurs over the flap height, while the drag contribution occurs mainly at the distal end.

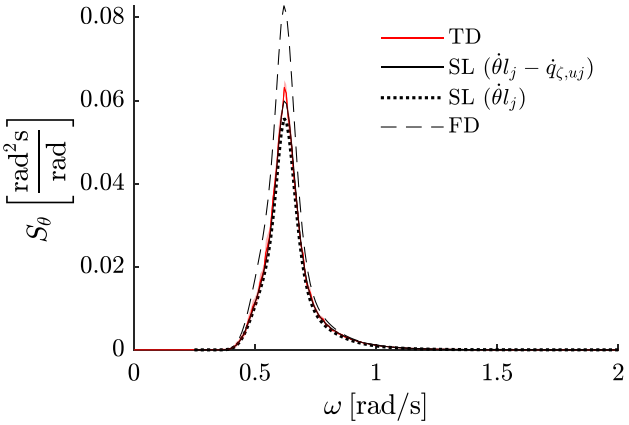

(a) PSD of angular displacement ($T_p = 10$ s).

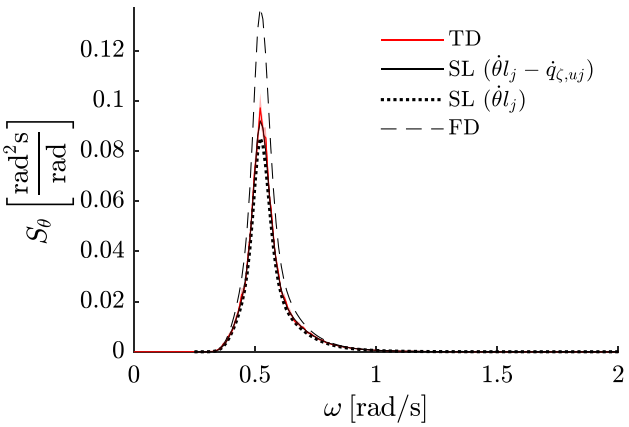

(b) PSD of the angular displacement ($T_p = 12$ s).

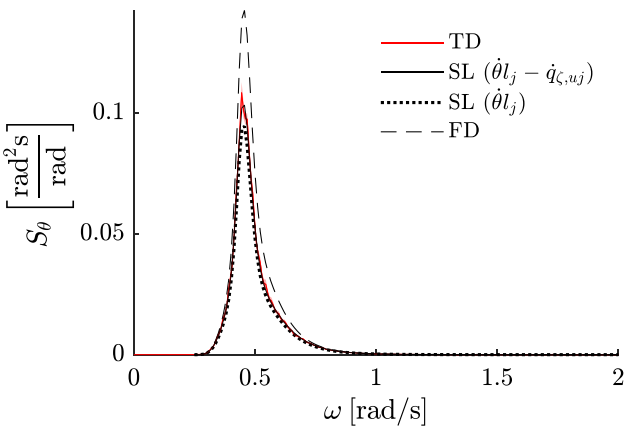

(c) PSD of the angular displacement ($T_p = 14$ s).

Fig. 11 PSD of the angular displacement for three T_p (10, 12, 14 s) and a $H_s = 1.5$ m. The shaded area denotes the standard deviation of the TD simulations

A similar trend between the influence of the excitation drag and damping drag components occurred over different significant wave heights. Figure 13 shows the mean power

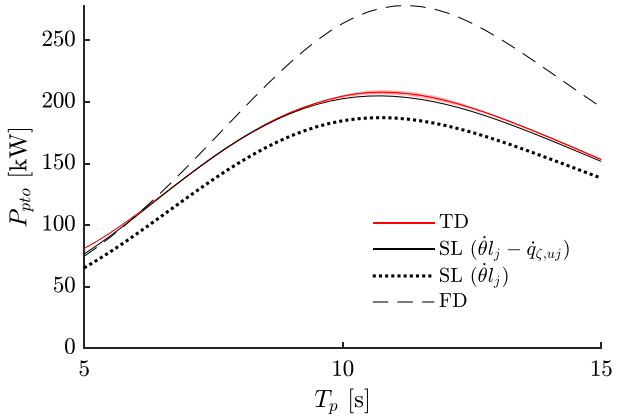

Fig. 12 Power absorbed by the OWSC as a function of T_p for a H_s = 1.5 m

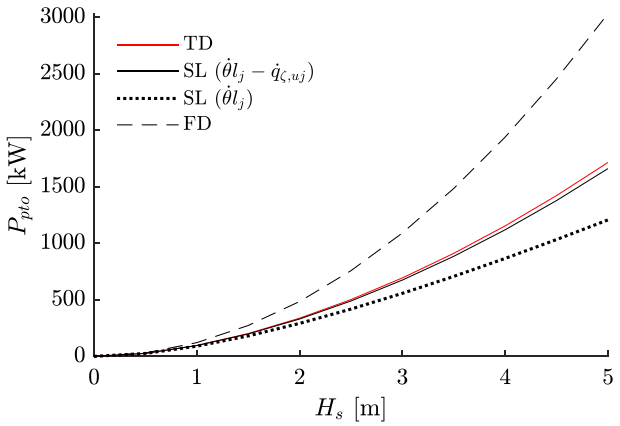

Fig. 13 Power absorbed by the OWSC as a function of H_s for a T_p = 12 s

Table 3 Comparison of mean simulation clock time

WEC	FD	SL($\dot{q} - \dot{q}_\zeta$)	SL($\dot{q}$)	TD (3000 cycles)
PA	0.002 [s]	0.084 [s]	0.075 [s]	223.1 [s]
OWSC	0.006 [s]	0.049 [s]	0.023 [s]	294.2 [s]

absorbed by the linear PTO using the four approaches as a function of the wave height and $T_p = 12$ s. For the conditions simulated, the SL ($\dot{\theta}l_j$) underestimated the power absorbed by 15.6% ± 8.3% compared to the SL ($\dot{\theta}l_j - \dot{q}_{\zeta,uj}$) model. Like the PA case, the estimations using the relative velocity were found to be important across most of the significant wave heights simulated.

6 Discussion

The main advantage of the SL is the low computational cost, while producing reliable estimations of the response compared to its respective nonlinear TD simulations. For the range of conditions simulated for both devices, the SL required approximately 5–7 iterations to achieve a relative error of 0.1% between the equivalent linear coefficients. The TD simulations require long periods to meet the requirement of ergodicity, and different incoming wave profiles were performed for more smooth results. Table 3 shows the mean simulation clock time for both devices using the four different models, in which the calculations were performed using a standard desktop PC with Intel Core i7 processor (2.4 GHz) and 16 GB RAM. In general, the average simulation clock time of the SL models for both WECs was 3 orders of magnitude faster than the nonlinear TD simulations, which was also observed in previous works (Silva et al. 2020a, b). The differences in the mean simulation clock time between the SL models, with and without the wave velocity, were negligible.

For both WECs, different parameters of the device and sea state can impact the influence of the viscous drag term using the relative velocity, as demonstrated for different wave periods, wave heights and PTO damping coefficient (in Appendix A). In addition, the spectral representation of the irregular waves, such as Pierson Moskowitz, Bretschneider, and JONSWAP, also affect the influence of the viscous drag term and the response of the WEC.

The wave description used in this work follows the linear theory, and is characterized by a Gaussian distribution. However, it should be noted that severe sea states traveling to shallow waters tend to be non-Gaussian (Ochi 2005). Therefore, the validity of the approximation of the wave velocity with a Gaussian distribution must be analyzed further, and modifications to the described SL procedure must be applied. Note that the approach derived in this work can be extended for other offshore systems and DOFs in system motion by making the appropriate modifications (Berge and Penzien 1974; Housseine et al. 2015).

7 Conclusion

This work formalized the application of the SL technique to the viscous drag effect based on Morison's equation using the relative velocity between the structure and the wave. Two WECs were investigated: a heaving PA and an OWSC. For the PA case, the wave velocity was calculated at the center of the buoy, while for the OWSC, the wave velocity was calculated at a finite number of sections of

the discretized structure. Based on the derivations, there is an equivalent linear system, where the nonlinearity from the viscous drag term is approximated to an equivalent damping and equivalent excitation term.

In general, the effect of the nonlinear drag force and torque into the system dynamics were well captured across all sea states and for the two WEC systems. The SL results using the relative velocity obtained good agreements with the nonlinear TD simulations in terms of PDF and PSD of the velocities (structure, wave, and relative), PSD of the displacement (vertical and angular) and power absorbed by the PTO system. For the PA simulated, the viscous drag force showed to be more important for lower periods and for regions close to resonance, where the wave velocity is higher and the device power absorption is more efficient. For such conditions, the velocity of the structure and wave velocity are comparable, and the SL using only the body velocity to describe the drag force/torque does not offer an appropriated approximation. Similar results were obtained for the simulated OWSC, where the viscous drag torque is more important at the distal end of the flap due to the distance from the hinged connection. At the distal end, the magnitude of the wave and flap motion are comparable and the SL using only the flap velocity losses representativeness.

The importance of the viscous drag using the relative velocity depends on the parameters of the simulation for the device and sea states, which can increase or decrease the difference between both SL models. Also, the relevance of the excitation term depends on the magnitude of the wave and the phase with the excitation force/torque. For example, the viscous drag excitation was more relevant to the OWSC because the excitation term is nearly in-phase with the wave component of the viscous drag term and the wave excitation drag term occurs over the flap height. As a result, the SL model using only the structure velocity underestimated the power produced for the OWSC.

Like other numerical codes, the verification and validation must be conducted to verify the real contribution of the viscous drag effects using the relative motion of the structure with respect to the fluid flow field. This work performed a verification of the proposed formulation using nonlinear TD simulation. However, validation against experimental tests or high-fidelity CFD is necessary for a better selection of the drag coefficient (C_D), which is a source of uncertainty. Regarding the technique, the proposed formulation offers a reliable estimate of the system dynamics compared to TD, while maintaining a computational cost compared to traditional FD models. Hence, the SL can be a valuable tool for optimization procedures, as shown in Sergiienko et al. (2020).

Acknowledgements L. S. P. da Silva acknowledges the Australia–China Science and Research Fund, Australian Department of Industry, Innovation and Science; and the Adelaide Graduate Centre, the University of Adelaide. C.P. Pesce acknowledges a CNPq Research Grant, nr. 308230/2018-3.

Appendix A: PTO damping selection

For both devices, the PTO damping is selected to optimize the power absorption for the condition specified based on the characteristics of the device. It is important to notice that the differences between both SL models (using the relative velocity and only the body velocity) may be observed over the entire range of conditions simulated (see Figs. 14 and 15).

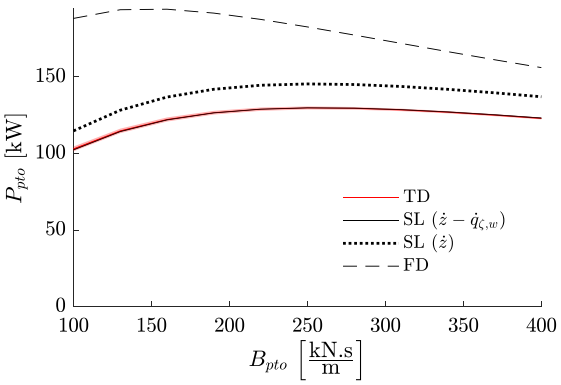

Fig. 14 Power absorbed by the PA for a range of B_{pto} ($T_{\text{p}} = 7.5$ s and $H_{\text{s}} = 3$ m)

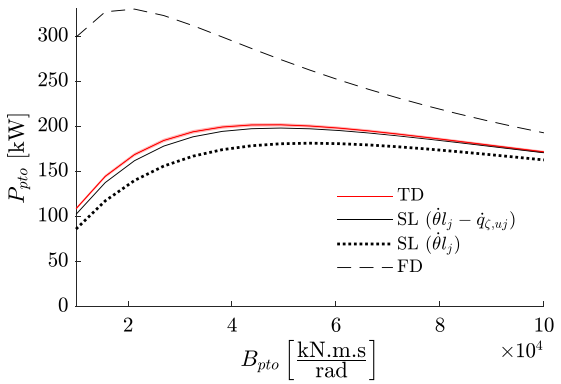

Fig. 15 Power absorbed by the OWSC for a range of B_{pto} ($T_{\text{p}} = 12$ s and $H_{\text{s}} = 1.5$ m)

References

Babarit A, Delhommeau G (2015) Theoretical and numerical aspects of the open source BEM solver NEMOH. In: 11th European Wave and Tidal Energy Conference (EWTEC2015), Nantes, France

Babarit A, Hals J, Muliawan MJ, Kurniawan A, Moan T, Krokstad J (2012) Numerical benchmarking study of a selection of wave energy converters. Renew Energy 41:44–63

Bacelli G, Ringwood JV (2014) Nonlinear optimal wave energy converter control with application to a flap-type device. IFAC Proc Vol 47(3):7696–7701

Bearman PW, Downie MJ, Graham JMR, Obasaju ED (1985) Forces on cylinders in viscous oscillatory flow at low Keulegan-Carpenter numbers. J Fluid Mech 154:337–356

Berge B, Penzien J (1974) Three-dimensional stochastic response of offshore towers to wave forces. In: Offshore Technology Conference, OTC, Houston, Texas

Davidson J, Costello R (2020) Efficient nonlinear hydrodynamic models for wave energy converter design A scoping study. J Mar Sci Eng 8(1):35

Folley M (2016) Spectral-domain models. In: Numerical modelling of wave energy converters. Elsevier, Berlin, pp 67–80

Folley M, Whittaker T (2010) Spectral modelling of wave energy converters. Coast Eng 57(10):892–897

Giorgi G, Penalba M, Ringwood J (2016) Nonlinear hydrodynamic force relevance for different wave energy converter types. In: Proceedings of the 3rd Asian wave and tidal energy conference, pp 154–162, Singapore

Giorgi G, Ringwood JV (2018) Comparing nonlinear hydrodynamic forces in heaving point absorbers and oscillating wave surge converters. J Ocean Eng Mar Energy 4(1):25–35

Housseine CO, Monroy C, de Hauteclocque G (2015) Stochastic linearization of the Morison equation applied to an offshore wind turbine, In: ASME 2015 34th international conference on ocean, offshore and arctic engineering, American Society of Mechanical Engineers, St. John's, Newfoundland, Canada

Journée JMJ, Massie WW (2000) Offshore Hydromechanics: Course OE4630, TU Delft

Keulegan GH, Carpenter LH (1956) Forces on cylinders and plates in an oscillating fluid: US Department of Commerce. NBS report, 4821, National Bureau of Standards

Molin B (2002) Hydrodynamique des structures offshore. Editions Technip, Paris

Morison JR, O'Brien MP, Johnson JW, Schaaf SA (1950) The force exerted by surface waves on piles. J Petrol Technol 2(05):149–154

Naess A, Pisano AA (1997) Frequency domain analysis of dynamic response of drag dominated offshore structures. Appl Ocean Res 19(5–6):251–262

Newman JN (2018) Marine hydrodynamics. MIT Press, Cambridge

Ochi MK (2005) Ocean waves: the stochastic approach, vol 6. Cambridge University Press, Cambridge

Perez T, Fossen TI (2009) A Matlab toolbox for parametric identification of radiation-force models of ships and offshore structures. Model Identif Control 30:1–15

Roberts JB, Spanos PD (2003) Random vibration and statistical linearization. Courier Corporation, Mineola, New York

Sergiienko NY, Neshat M, Silva LSP, Alexander B, Wagner M (2020) Design optimisation of a multi-mode wave energy converter, In: ASME 2020 39th International Conference on Ocean, Offshore and Arctic Engineering, American Society of Mechanical Engineers, Fort Lauderdale, FL, USA

Silva LSP (2019) Nonlinear stochastic analysis of wave energy converters via statistical linearization, MSc thesis, University of São Paulo, Brazil

Silva LSP, Morishita HM, Pesce CP, Gonçalves RT (2019) Nonlinear analysis of a heaving point absorber in frequency domain via statistical linearization, In: ASME 2019 38th International Conference on Ocean, Offshore and Arctic Engineering, American Society of Mechanical Engineers, Glasgow, Scotland, UK

Silva LSP, Sergiienko N, Pesce CP, Ding B, Cazzolato B, Morishita HM (2020a) Stochastic analysis of nonlinear wave energy converters via statistical linearization. Appl Ocean Res 4:5

Silva LSP, Sergiienko NY, Cazzolato BS, Ding B, Pesce CP, Morishita HM (2020b) , Nonlinear analysis of an oscillating wave surge converter in frequency domain via statistical linearization, In: ASME 2020 39th International Conference on Ocean, Offshore and Arctic Engineering, American Society of Mechanical Engineers, Fort Lauderdale, FL, USA

Spanos PD, Arena F, Richichi A, Malara G (2016) Efficient dynamic analysis of a nonlinear wave energy harvester model. J Offshore Mech Arctic Eng 138(4):041901

Todalshaug JH, Babarit A, Kurniawan A, Moan T (2011) 'The NumWEC project. Numerical estimation of energy delivery from a selection of wave energy converters', Report, Ecole Centrale de Nantes & Norges Teknisk-Naturvitenskapelige Universitet

Wolfram J (1999) On alternative approaches to linearization and Morison's equation for wave forces. Proc R Soc Lond Ser A Math Phys Eng Sci 455:2957–2974